


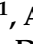




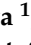

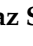
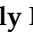

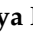


Article

Modulating the Inclusive and Coordinating Ability of Thiacalix[4]arene and Its Antenna Effect on Yb³⁺-Luminescence via Upper-Rim Substitution

Sergey N. Podyachev ^{1,*} , Svetlana N. Sudakova ¹ , Rustem R. Zairov ¹ , Victor V. Syakaev ¹ , Alexey N. Masliy ² , Michal Dusek ³ , Aidar T. Gubaidullin ¹ , Alexey P. Dovzhenko ⁴ , Daina N. Buzyurova ¹ , Dmitry V. Lapaev ⁵ , Gulnaz Sh. Mambetova ¹ , Vasily M. Babaev ¹ , Andrey M. Kuznetsov ²  and Asiya R. Mustafina ¹ 

¹ Arbuzov Institute of Organic and Physical Chemistry, FRC Kazan Scientific Center of RAS, Arbuzov Str. 8, 420088 Kazan, Russia

² Department of Inorganic Chemistry, Kazan National Research Technological University, K. Marx Str. 68, 420015 Kazan, Russia

³ Institute of Physics of the Czech Academy of Sciences, Na Slovance 2, 182-21 Prague, Czech Republic

⁴ Department of Physical Chemistry, Kazan (Volga Region) Federal University, Kremlyovskaya Str. 18, 420008 Kazan, Russia

⁵ Zavoisky Physical-Technical Institute, FRC Kazan Scientific Center of RAS, Sibirsky Tract 10/7, 420029 Kazan, Russia

* Correspondence: spodyachev@iopc.ru



Citation: Podyachev, S.N.; Sudakova, S.N.; Zairov, R.R.; Syakaev, V.V.; Masliy, A.N.; Dusek, M.; Gubaidullin, A.T.; Dovzhenko, A.P.; Buzyurova, D.N.; Lapaev, D.V.; et al. Modulating the Inclusive and Coordinating Ability of Thiacalix[4]arene and Its Antenna Effect on Yb³⁺-Luminescence via Upper-Rim Substitution. *Molecules* **2022**, *27*, 6793. <https://doi.org/10.3390/molecules27206793>

Academic Editor: Vito Lippolis

Received: 25 August 2022

Accepted: 30 September 2022

Published: 11 October 2022

Publisher's Note: MDPI stays neutral with regard to jurisdictional claims in published maps and institutional affiliations.



Copyright: © 2022 by the authors. Licensee MDPI, Basel, Switzerland. This article is an open access article distributed under the terms and conditions of the Creative Commons Attribution (CC BY) license (<https://creativecommons.org/licenses/by/4.0/>).

Abstract: The present work introduces the series of thiacalix[4]arenes (H₄L) bearing different upper-rim substituents (R = H, Br, NO₂) for rational design of ligands providing an antenna-effect on the NIR Yb³⁺-centered luminescence of their Yb³⁺ complexes. The unusual inclusive self-assembly of H₃L[−] (Br) through Br . . . π interactions is revealed through single-crystal XRD analysis. Thermodynamically favorable formation of dimeric complexes [2Yb³⁺:2HL^{3−}] leads to efficient sensitizing of the Yb³⁺ luminescence for H₄L (Br, NO₂), while poor sensitizing is observed for ligand H₄L (H). X-ray analysis of the single crystal separated from the basified DMF solutions of YbCl₃ and H₄L(NO₂) has revealed the transformation of the dimeric complexes into [4Yb³⁺:2L^{4−}] ones with a cubane-like cluster structure. The luminescence characteristics of the complexes in the solutions reveal the peculiar antenna effect of H₄L(R = NO₂), where the triplet level at 567 nm (17,637 cm^{−1}) arisen from ILCT provides efficient sensitizing of the Yb³⁺ luminescence.

Keywords: calix[4]arenes; Yb³⁺ complexes; luminescence; halogen-bonding; X-ray analysis

1. Introduction

Calix[n]arenes and their thia-analogues continue to excite interest as a promising basis for design and synthesis of lanthanide complexes, which were successfully applied in developing nanosensors and contrasting agents [1,2]. The main advantage of a cyclophanic backbone is the feasibility of the structural diversifications, which allows embedding of different groups, in turn allowing either complex ability of the calixarene derivatives or tuning their acid/base and complexing properties through electronic effects of the substituents [3,4]. Moreover, the presence of the cyclophanic cavity results in unique inclusive complex formation mainly driven by the electron-donating ability of the cavity [5,6]. The present work is focused on upper-rim substituted thiacalix[4]arenes since preorganization of the four phenolic moieties provides excellent chelating properties towards lanthanide ions, followed by ligand-to-lanthanide energy transfer [1,7–9]. It is worth noting that upper-rim substitution of thiacalix[4]arenes was already documented as the tool to both increase their water solubility [9,10] and modify their sensitizing effect on lanthanide-centered luminescence [1,7–9]. In particular, embedding of the bromine-substituents onto the upper rim of thiacalix[4]arenes allows to modify the ligand-centered triplet level responsible for

feeding of the excited lanthanide-centered levels [8]. Incorporation of nitro-groups onto the upper rim of thiacalix[4]arene has also been reported [11–14].

Ytterbium compounds exhibiting near-infrared (NIR) luminescence are widely applied building blocks of nanomaterials for bioimaging and photothermal therapy [15–22]. This is due to the fact that Yb^{3+} -centered luminescence exhibits the greatest intensity among other NIR-emitting lanthanide ions [23], which, in turn, derives from the large energy gap, $10,250\text{ cm}^{-1}$, between its emitting level and the ground state [24]. The poor feeding of the excited ${}^2\text{F}_{5/2}$ -level of Yb^{3+} due to forbiddance of f - f transitions raises a question of their feeding through ligand-to-metal [25,26] or metal-to-metal energy transfer and minimizing of radiationless transitions from the excited Yb^{3+} -level to lower laying vibrational levels of ligands [27–29]. The reports of Iki et al. [30–32] highlight the advantage of the thiacalix[4]arene backbone in developing NIR-luminescent Yb^{3+} complexes due to the specific rigid inner-sphere environment resulting from the sandwich-like coordination of the Yb^{3+} ions between two phenolate rims of the thiacalix[4]arene derivatives.

However, an impact of the upper-rim substitution of thiacalix[4]arenes by the bromine and nitro-groups on the developing of bright NIR Yb^{3+} -centered luminescence has not been highlighted. A combination of electron-withdrawing (NO_2) and electron-donating moieties (OH , O^-) in thiacalix[4]arene molecules should produce an intraligand charge transfer (ILCT) absorption band in the visible range similar to that in the electronic spectra of nitrophenolates [33]. Literature data demonstrate fine examples of convenient excitation of Yb^{3+} NIR luminescence by means of an ILCT absorption band in the visible range [25,26,34]. Thus, it is worth assuming that combination of the rigid inner-sphere ligand environment of Yb^{3+} ions with excitation of an Yb^{3+} -centered luminescence by means of an ILCT absorption band can be a tool to develop bright Yb^{3+} -centered luminescence.

The present work represents thiacalix[4]arenes $\text{H}_4\text{L}(1-3)$ (Figure 1) with different upper-rim substituents ($\text{R} = \text{H}$, Br and NO_2). The structural variation in the upper-rim substituents is aimed to highlight their impact on producing unique supramolecular structures, in turn derived from inclusive or coordinating abilities of the bromo- and nitro-substituted thiacalix[4]arenes. Such structure variation is also aimed at distinguishing different structure effects on Yb^{3+} -centered luminescence of the corresponding complexes, including: (1) structure rigidity effect derived from bulky substituents (Br , NO_2); (2) interaction of the lone pairs of NO_2 group with π^* orbitals of the aromatic ring, which is known to quench Eu^{3+} and Tb^{3+} luminescence through shortening of the triplet excited state lifetime [35]; (3) participation of the triplet level arisen from the ILCT in the feeding of the low-energy excited states of Yb^{3+} .

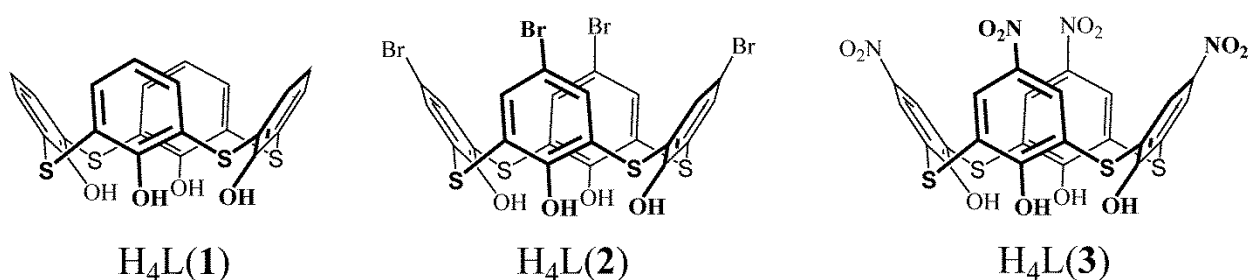


Figure 1. Thiacalix[4]arenes $\text{H}_4\text{L}(1-3)$ studied in this work.

The unique supramolecular structures of bromo-substituted thiacalix[4]arene and the ytterbium complex of nitro-substituted thiacalix[4]arene determined by single-crystal X-ray diffraction (XRD) data will be discussed in correlation with the literature data and experimental results on complexation of Yb^{3+} with thiacalix[4]arenes in DMF solutions. The coordination modes of Yb^{3+} in the complexes will be revealed by computational modelling. Steady state and time-resolved Yb^{3+} -centered luminescence will be correlated with both spectral properties and structural features of the ligands in order to recognize the impact of different factors, including the ILCT, on the luminescence of the complexes.

2. Results and Discussion

2.1. UV–Vis Absorption Behavior of $H_4L(3)$ and Crystal Structure of $H_3L(2)^-$

Discussion of the complex ability and antenna-effect of $H_4L(1-3)$ ligands in basified DMF solutions should be preceded by analysis of their acid–base behavior revealed through their spectral behavior at different concentrations of TEA. Both spectral and acid–base behaviors of $H_4L(1,2)$ in DMF solutions have already been published [7,8], and a correlation between deprotonation and spectral changes for $H_4L(3)$ was reported in aqueous solutions [12,13].

The electronic absorption spectra of **3** recorded in the neutral and basified DMF solutions are represented in Figure 2a. The enhanced electronic absorbance at 340–400 nm revealed from the spectrum of **3** in the neutral DMF solution (Figure 2a) is explained by the enhanced first step deprotonation of $H_4L(3)$ since similar spectral behavior of $H_4L(3)$ in the aqueous solutions was correlated with $pK_1 = 2.75$ [13]. The enhanced acidity of $H_4L(3)$ derives from both its cyclophanic structure and the electron-withdrawing effect of *p*-nitro-substituents, which differentiates $H_4L(3)$ from $H_4L(1,2)$.

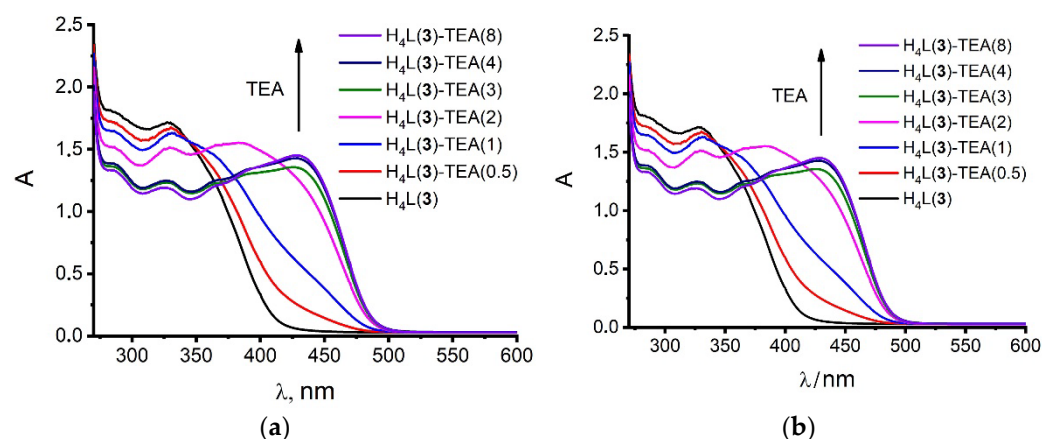


Figure 2. (a) UV–Vis spectra and (b) the absorbance values (A) ($\lambda = 430$ nm) in neutral and basified DMF solutions of $H_4L(3)$ ($C_{H_4L} = 0.05$ mM) at the varied TEA/L (0–8) molar ratio.

The low-energy band of $H_4L(3)$ is both red-shifted and more intensive (Figure 2a) than the shoulder at 340 nm for $H_4L(2)$ [8], which, in turn, is more pronounced than that of $H_4L(1)$ [8]. The spectral behavior of $H_4L(3)$ in the basified DMF solutions is characterized by the appearance of electronic absorbance at ~ 450 – 500 nm (Figure 2a). The red-shifting of the low-energy band of $H_4L(3)$ versus those of $H_4L(1,2)$ derives from the well-known high electron-withdrawing effect of nitro-substituents, resulting in the appearance of the ILCT absorption band. It is worth noting that the electronic absorption of $H_4L(3)$ in the basified DMF solutions is in the longer wavelengths range, ~ 450 – 500 nm compared to the absorption of *p*-nitrophenol (~ 400 – 450 nm) in the alkaline solutions [33]. Thus, the cyclophanic structure of $H_4L(3)$ favors lower energy transitions, along with the effect of the *p*-nitro-substituents, which is the reason for the peculiar spectral behavior of H_4L versus that of *p*-nitrophenol. As is evident from the titration plot in Figure 2b, two-step deprotonation of $H_4L(3)$ is realized in the basified DMF solutions, while only one-step deprotonation was reported for $H_4L(1,2)$ [7,8].

The above-mentioned deprotonation of the phenolic rims of $H_4L(1-3)$ facilitates the electron-donating ability of their cavities, which promotes unique intermolecular inclusive interactions and coordination of metal ions. These interactions are clearly demonstrated by XRD analysis of the single crystals ($H_3L(2)^- \cdot (CH_3)_2NH_2^+ \cdot DMF$) grown from the DMF solutions of **2** basified by dimethylamine (Figure 3). The thiacalixarene molecule in an almost perfect *cone* conformation with close values of dihedral angles of opposite aromatic rings is located in the general position of the triclinic unit cell (Figure 3). However, the molecule loses its own C_4 symmetry due to its transformation into salt form, interaction with the

solvent molecule (Figure 3a) and specific inclusive interactions (Figure 3b). The crystal structure data (Table S1) and the parameters of the intra- and intermolecular interactions (Tables S2 and S3 and Figures S1–S4) are represented in the Supplementary Materials.

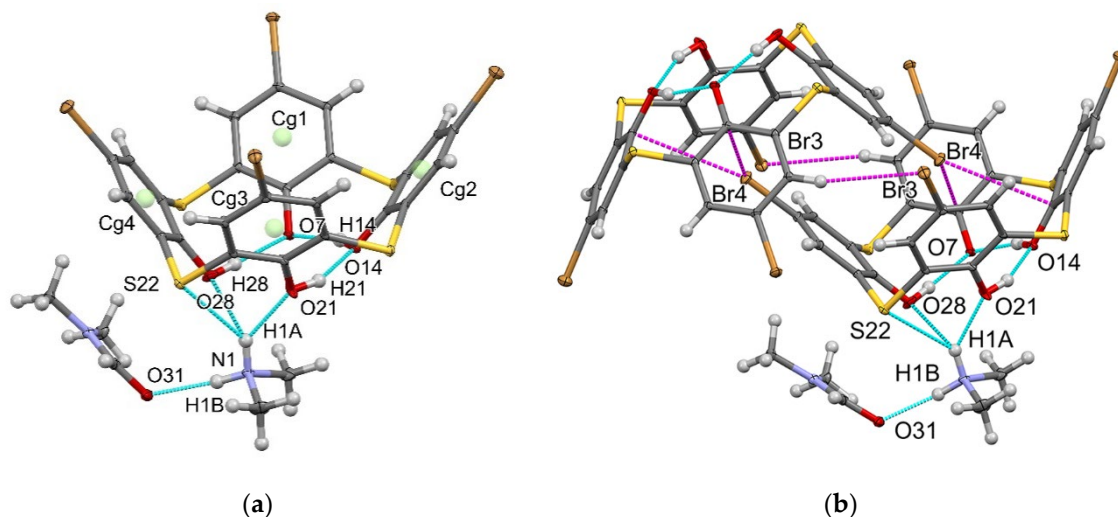


Figure 3. (a) O-H ... O, N-H ... O and N-H ... S hydrogen bonds (blue dashed lines) (a) and Br ... π ; (b) C-H ... Br interactions (magenta dashed lines) in the crystal $\text{H}_3\text{L}(2)^- \cdot (\text{CH}_3)_2\text{NH}_2^+ \cdot \text{DMF}$.

An interesting feature of the intermolecular interaction revealed in single crystals is formation of peculiar centrosymmetric dimers of thiacalix[4]arenes (Figure 3b). Substituent Br3 participates in the strong C-H ... Br interaction with the hydrogen H3 of the phenyl ring of the neighboring molecule; the H3 ... Br3 distance is 3.03 Å. Pairwise incorporation of the bromine substituents designated as Br4 of one molecule into the cavity of another can be stabilized by four Br ... π contacts with the four phenyl rings of the thiacalix[4]arene. However, in accordance with the IUPAC criteria [36], only one (Cg2(C9 \div C14) ... Br4) of the four contacts can be called a halogen bond since the rest of them do not follow the rule of directionality of such bonds. Moreover, two of them have distances between the centers of the bromine and the nearest carbon atoms slightly more than the sum of their van der Waals radii (see Table S3 in Supplementary Materials). However, the formal criteria for such interactions used in the PLATON program [37] allows to consider all the contacts to the Br ... π type (for the contact parameters, see Table S3).

It is worth noting the diversity of the Br ... π contacts: in particular, the C-Br bond is directed to carbon C14 (Cg2(C9 \div C14) ... Br4), while, in the contact Cg1(C2 \div C7) ... Br4, the bromine atom is in an intermediate position between the center of the aromatic cycle and atom C7. In the case of contacts Cg3(C16 \div C21) ... Br4 and Cg4(C23 \div C28) ... Br4, the bromine atom is closer to the centers of aromatic rings, which are electron-deficient regions. The aforesaid provides one more example of the unique ability of the bromine substituents to interact with both nucleophilic and electrophilic centers, which has gained great attention in the last decade [38].

The revealed short Br ... π contacts are predominantly driven by polarized electrostatic attractions between the electron-deficient bromo-substituents and the electron donating cavity of $\text{H}_3\text{L}^-(2)$ as a Lewis base [39,40]. It is worth noting that halogen bonds have already been highlighted as the driving force of inclusion of halogen-substituted benzenes into the cavities of calix[4]arene derivatives [41]. A search of the Cambridge Structural Database (CSD version 5.43, March 2022 release) for all structures containing upper-rim halogen substituted thia- and calix[4]arenes (68 hits) reveals the only example of dimeric or cog-like self-inclusion of distal substituted dibromocalix[4]arene bearing the two propoxy groups on the lower-rim [42]. This indicates that the present inclusive self-assembly based on halogen bonds is rather rare. Moreover, dimeric self-assembly is also stabilized by the C-H ... Br interaction driven by the electron donating capacity of

the bromo-substituents (Figure 3b and S1). Thus, the Janus-like nature of the bromine substituents provides additional interactions, which, along with S... π and π ... π interactions, form the one-dimensional supramolecular motif (Figure S1). Such chains are bound in a perpendicular direction due to Br... π and C-H...Br contacts (Figure S2), forming a two-dimensional supramolecular motif—a layer of thiacalixarene dimeric fragments, where the dimeric structure shown in Figure 3b serves as a supramolecular synthon. Translation of such synthon in three directions forms a crystal packing as a whole (Figures S3 and S4). It is worth noting that the supramolecular packing is characterized by a sufficiently high packing factor of 0.717, which is closer to the upper limit of the packing factor values for crystals of organic compounds (0.65–0.75).

2.2. Complex Formation of $H_4L(1-3)$ with Yb^{3+} Ions

Compounds $H_4L(1,2)$, previously represented as efficient ligands for Tb^{3+} ions, provide their tight coordination followed by efficient sensitizing of terbium-centered luminescence [7,8]. Discussion of the complex formation of ligand $H_4L(3)$ in solutions is worth preceding by a presentation of the structure determined by XRD analysis of the single crystals grown from basified DMF solution containing $H_4L(3)$ and Yb^{3+} ions in a 1:1 molar ratio.

The single crystals suitable for XRD analysis were grown through several months staying of the basified DMF solutions of $YbCl_3$ and $H_4L(3)$ mixed in a 1:1 ratio, while no single crystals appeared in the same conditions for ligands $H_4L(1,2)$. Moreover, in the case of the $Yb(NO_3)_3$, we could not succeed in obtaining any crystals.

X-ray analysis of the separated single crystal revealed the large and strongly disordered structure in the monoclinic P21/n space group. A detailed description of the crystal structure data is in Supplementary Materials (Figures S5 and S6 and Table S4). The cell unit consists of two individual complexes in its composition with 2:1 (Yb:L) stoichiometry, although, as has been aforesaid, $YbCl_3$ and $H_4L(3)$ were mixed in a 1:1 ratio (Figure 4). Both of them contain a rather specific dimeric cubane-like structure of complex. The cluster coordination of four Yb^{3+} ions with eight phenolates of two completely deprotonated *p*-nitro-thiacalix[4]arene anions (L^{4-}) is stabilized by the bridge-like coordination of chloride ions with the coordination number of Yb^{3+} ions equal to 6 and 7, according to Figure 4. Such values are rather scarce in comparison with coordination numbers 8 and 9 predominantly reported in the literature [43]. However, the data quality is insufficient to reveal such structural details as a location and number of water molecules supporting the structure.

Stabilization of transition metal ions clusters through coordination by thiacalix[4]arenes is well-represented by the review [44]. However, the cubane-like lanthanide coordination ($Ln = Gd^{3+}$, Eu^{3+} and Tb^{3+}) has been found only for sulfonylcalix[4]arene, where the cluster motif is supported by coordination of the lanthanide ions via both phenolates and sulfonyl oxygen atoms along with four bridging acetate ligands [44,45].

Both stoichiometry and structure of the cubane-like dimeric complex of Yb^{3+} with ligand $H_4L(3)$ significantly differ from those of the dimeric terbium complexes formed by ligands 1 and 2 in the DMF solutions [7,8]. Thus, the revealed dimeric structure may either derive from the complex formation mode in solutions or be mainly affected by the crystal packing forces. However, the lanthanide contraction may be one more reason for specificity in the coordinative behavior of Yb^{3+} versus its counterparts from the middle of the lanthanide series. Therefore, the complex formation of $H_4L(3)$ with Yb^{3+} ions will be represented along with that of $H_4L(1,2)$ in the DMF solutions.

The intraligand electronic absorbance of $H_4L(1-3)$ is a convenient tool to reveal and compare their complex formation abilities towards lanthanide ions. The UV-Vis spectral data calculated and represented in the form of the Job's plots in Figure 5a demonstrate no specificity of Yb^{3+} complex formation with ligands $H_4L(1)$ and $H_4L(2)$ in comparison with earlier obtained data for their Tb^{3+} complexes [7,8]. The complex formation of Yb^{3+} is accompanied by the deprotonation of two and three protons under their complex formation with $H_4L(1)$ and $H_4L(2)$ (Figure 5b), which is also in good agreement with the terbium complex formation.

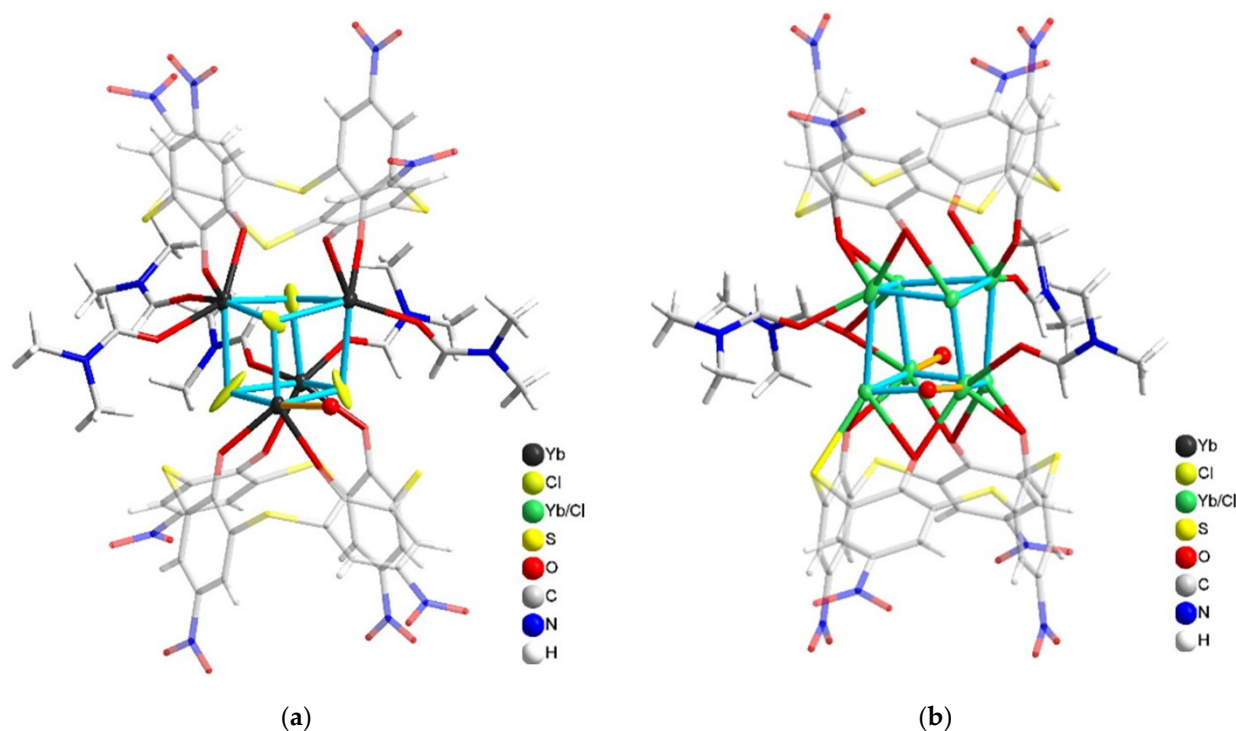


Figure 4. Ligands coordinated to the Yb_4Cl_4 “cube”: (a) with separated Yb and Cl positions. Cl atoms are disordered and not bonded to ligands; (b) with mixed Yb and Cl positions. L^{4-} anions are plotted semi-transparent. A water molecule is represented by an oxygen atom plotted as a red ball.

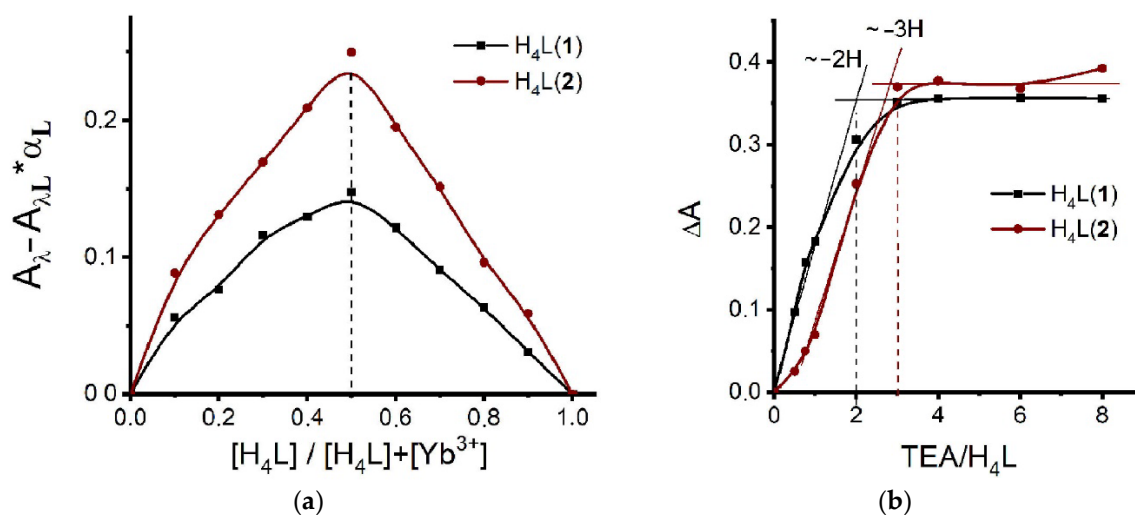


Figure 5. The Job's plot profiles of DMF solutions at the varied $\text{H}_4\text{L}:\text{Yb}^{3+}$ molar ratios: (a) $\text{H}_4\text{L}(1)$ ($\lambda = 340$ nm), $\text{H}_4\text{L}(2)$ ($\lambda = 350$ nm) ($[\text{H}_4\text{L}] + [\text{Yb}^{3+}] = 0.1$ mM, L:TEA (1:8)); (b) ΔA of the DMF solutions of H_4L with $\text{Yb}(\text{NO}_3)_3$ at the varied TEA:L molar ratios: $\text{H}_4\text{L}(1)$ ($\lambda = 340$ nm), $\text{H}_4\text{L}(2)$ ($\lambda = 350$ nm). $C_{\text{Yb}^{3+}} = C_{\text{H}_4\text{L}} = 0.1$ mM.

It should be noted that similar data for *p*-nitro-thiacalix[4]arene $\text{H}_4\text{L}(3)$ have not been reported. The addition of Yb^{3+} to the basified solution of $\text{H}_4\text{L}(3)$ results in increased absorbance at 400 nm with the disappearance of the lower energy absorption bands at 450–500 nm (Figure 6a). Such spectral behavior provides a clear indication of Yb^{3+} coordination via the lower phenolic rim of H_4L as the reason for restricted charge transfer from phenolate to nitro-groups. The quantitative analysis of the spectral changes resulting from the concentration variation in both $\text{H}_4\text{L}(3)$ and $\text{Yb}(\text{NO}_3)_3$ through the Job-plotting

(Figure 6b) indicates that the complex formation of Yb^{3+} ions with $\text{H}_4\text{L}(3)$ in the basified DMF solutions predominantly occurs in 1:1 stoichiometry. However, similar with $\text{H}_4\text{L}(1, 2)$, the non-symmetrical shape of the Job plot (Figures 5a and 6b) indicates that the 1:1 stoichiometry is contributed by the complex forms with 2:1 (Yb:L) stoichiometry. It is worth noting that the Job plots are indistinguishable in the solutions of $\text{Yb}(\text{NO}_3)_3$ and YbCl_3 , which points to predominance of the 1:1 stoichiometry in the recently prepared basified DMF solutions (Figure S7).

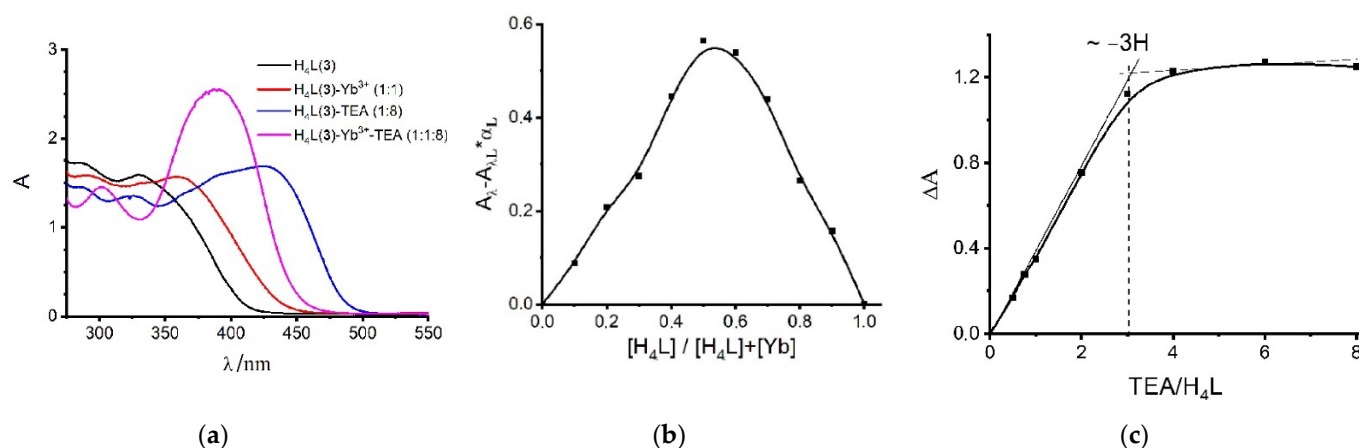


Figure 6. (a) UV-Vis absorption spectra of $\text{H}_4\text{L}(3)$ ($C_L = 0.05$ mM) in DMF; $\text{H}_4\text{L}(3)$ with $\text{Yb}(\text{NO}_3)_3$ ($C_{\text{Yb}^{3+}} = 0.05$ mM) ($\text{H}_4\text{L}(3)\text{-Yb}^{3+}$ (1:1)); $\text{H}_4\text{L}(3)$ with TEA ($C_{\text{TEA}} = 0.4$ mM) ($\text{H}_4\text{L}(3)\text{-TEA}$ (1:8)); $\text{H}_4\text{L}(3)$ with $\text{Yb}(\text{NO}_3)_3$ ($C_{\text{Yb}^{3+}} = 0.05$ mM) and TEA ($C_{\text{TEA}} = 0.4$ mM) ($\text{H}_4\text{L}(3)\text{-Yb}^{3+}\text{-TEA}$ (1:1:8)); (b) the Job's plot profiles of DMF solutions at the varied $\text{H}_4\text{L}(3)\text{:Yb}^{3+}$ molar ratios: ($\lambda = 400$ nm) ($[\text{Yb}^{3+}] + [\text{H}_4\text{L}] = 0.05$ mM, $[\text{H}_4\text{L}]\text{:TEA}$ (1:8)); (c) ΔA of the DMF solutions of $\text{H}_4\text{L}(3)$ with $\text{Yb}(\text{NO}_3)_3$ at the varied TEA:L molar ratio ($\lambda = 400$ nm, $C_{\text{Yb}^{3+}} = C_L = 0.05$ mM).

Thus, similar to the other thiacalix[4]arenes $\text{H}_4\text{L}(1,2)$, the 1:1 complex stoichiometry is predominant in the complex formation of $\text{H}_4\text{L}(3)$ with Yb^{3+} , followed by deprotonation of three phenolic moieties (Figure 6c). It is interesting that longer storage of the solutions with YbCl_3 resulted in obtaining crystals having the 2:1 stoichiometry. In accordance with Le Chatelier's principle, the phase separation of the crystals is the main driving force for both further deprotonation of the ligand and transformation of the complex stoichiometry from 1:1 to 2:1. It is also worth noting that the DMF molecule caps the cyclophanic cavities, and it should be considered as one more factor for stabilizing the structure.

2.3. Diffusion NMR Spectroscopy

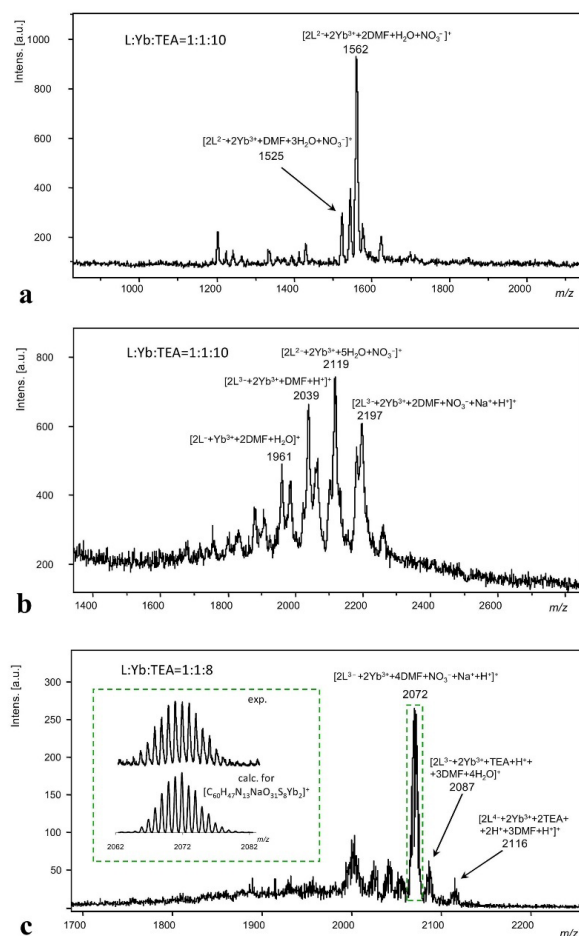
The NMR spectral changes of ligands $\text{H}_4\text{L}(1\text{--}3)$ resulted from their complex formation in alkalinized $\text{DMSO-}d^6$ solutions were analyzed for diamagnetic Lu^{3+} ions in order to exclude the broadening of signals due to the paramagnetic effect of Yb^{3+} ions. The interference of the signals arising from the different complex forms restricts the correct evaluation of self-diffusion coefficients in the case of $\text{H}_4\text{L}(1)$. Thus, the self-diffusion coefficients were obtained for the complexes with $\text{H}_4\text{L}(2,3)$ (Table 1). Their quantitative analysis allows estimating that the self-diffusion coefficient of ligand $\text{H}_4\text{L}(2)$ decreases by 16% under the complex formation with Lu^{3+} (Table 1), while in the case of La^{3+} , a more significant decrease (21%) was reported [8]. The self-diffusion coefficient for the thiacalix[4]arene $\text{H}_4\text{L}(3)$ under the complex formation with Lu^{3+} becomes lower by 14% (Table 1). According to the literature data, the decrease of D_s by ~25% testifies to the dimerization of the molecules in the solutions [46–48]. Therefore, the less pronounced decrease in self-diffusion coefficients D_s of ligands $\text{H}_4\text{L}(2,3)$ under the complex formation with Lu^{3+} versus La^{3+} ions indicates the greater contribution of the monomeric forms. In particular, the accumulation of dimeric complex forms is ~65% and 55% for ligands $\text{H}_4\text{L}(2)$ and $\text{H}_4\text{L}(3)$, correspondingly.

Table 1. Self-diffusion constants, hydrodynamic radii for ligands H₄L(2,3) (2.5 mM) in DMSO-*d*⁶ solutions before and after addition of Lu³⁺ (2.5 mM) and TEA (15 mM) at 303 K.

System (Molar Ratio)	Self-Diffusion Coefficients (10 ⁻¹⁰ m ² s ⁻¹)	Hydrodynamic Radii <i>r</i> _H (Å)
2	2.32	5.5
2-TEA (1:6)	2.31	5.3
2- Lu ³⁺ -TEA (1:1:6)	1.95	6.6
3	2.37	5.4
3-TEA (1:6)	2.32	5.5
3- Lu ³⁺ -TEA (1:1:6)	2.04	6.3

2.4. MALDI-TOF Mass Spectrometry Data

MALDI-TOF mass spectra were recorded for the mixtures Yb³⁺: L: TEA (1:1:8, 1:1:10) in DMF solutions with registration of positively charged ions (Figure 7). The intensive peaks at *m/z* = 1500–1600 assignable to the dimeric (2:2) complexes ([2L²⁻ + 2Yb³⁺ + DMF + 3H₂O + NO₃⁻]⁺, [2L²⁻ + 2Yb³⁺ + 2DMF + H₂O + NO₃⁻]⁺) are revealed for ligand **1** (Figure 7a). The intensive peaks at *m/z* 1900–2200 assignable to the monomeric ([2L⁻ + Yb³⁺ + 2DMF + H₂O]⁺) and dimeric complex forms ([2L²⁻ + 2Yb³⁺ + DMF + H⁺]⁺, [2L²⁻ + 2Yb³⁺ + DMF + H₂O + NO₃⁻]⁺, [2L³⁻ + 2Yb³⁺ + 2DMF + NO₃⁻ + Na⁺ + H⁺]⁺) (Figure 7b) are observed for ligand **2**. In turn, only the peaks at *m/z* 1950–2150 ([2L³⁻ + 2Yb³⁺ + 4DMF + NO₃⁻ + Na⁺ + H⁺]⁺, [2L³⁻ + 2Yb³⁺ + 3DMF + 4H₂O + TEA + H⁺]⁺) (Figure 7c) assignable to dimeric complexes are registered in the case of ligand **3**. Thus, the MALDI-TOF mass spectra confirm the tendency of ligands H₄L(1–3) to form dimeric complexes with Yb³⁺.

**Figure 7.** MALDI-TOF mass spectra of the H₄L-Yb³⁺-TEA (1:1:8, 1:1:10) system: L = (a) H₄L(1); (b) H₄L(2); (c) H₄L(3).

2.5. Computational Modeling of the Yb^{3+} Complexes with *p*-Nitrothiacalix[4]arene ($\text{H}_4\text{L}(3)$)

The DFT calculations were successfully applied in recognition of the impact of the complex stoichiometry and structure on its stability for the lanthanide complexes with the calix[4]arene and thiacalix[4]arene derivatives, including, in particular, the complexes with ligands $\text{H}_4\text{L}(1)$ and $\text{H}_4\text{L}(2)$ [7,8]. The DFT calculations of ytterbium complexes with ligand **3** are based on the previously reported thermodynamically favorable structures of Tb^{3+} complexes with ligands $\text{H}_4\text{L}(1)$ and $\text{H}_4\text{L}(2)$ with the assumption of the terbium coordination number (CN) being equal to 8. The CN-value of Yb^{3+} can be either 8 or 7 in accordance with the well-known “lanthanide contraction effect”. However, the literature data [49] reveal relatively small differences in the ionic radii of Yb^{3+} (1.125 Å) and Tb^{3+} (1.180 Å) ions. This, in turn, argues for the realization of CN = 8 for the Yb^{3+} complexes with $\text{H}_4\text{L}(3)$ in the solutions [50].

The diversity of the complex formation modes is represented by both monomeric (1:1) and dimeric (2:2) complex forms. The 1:1 complex formation leading to $[\text{YbHL}]$ can derive from the coordination of Yb^{3+} via either four oxygens of phenolic/phenolate lower rim of HL^{3-} (**3**) ($[\text{YbHL}(\text{DMF})_4]$ -**(I)** in Figure 8) or via two oxygen and one sulfur atom ($[\text{YbHL}(\text{DMF})_5]$ -**(II)** in Figure 8).

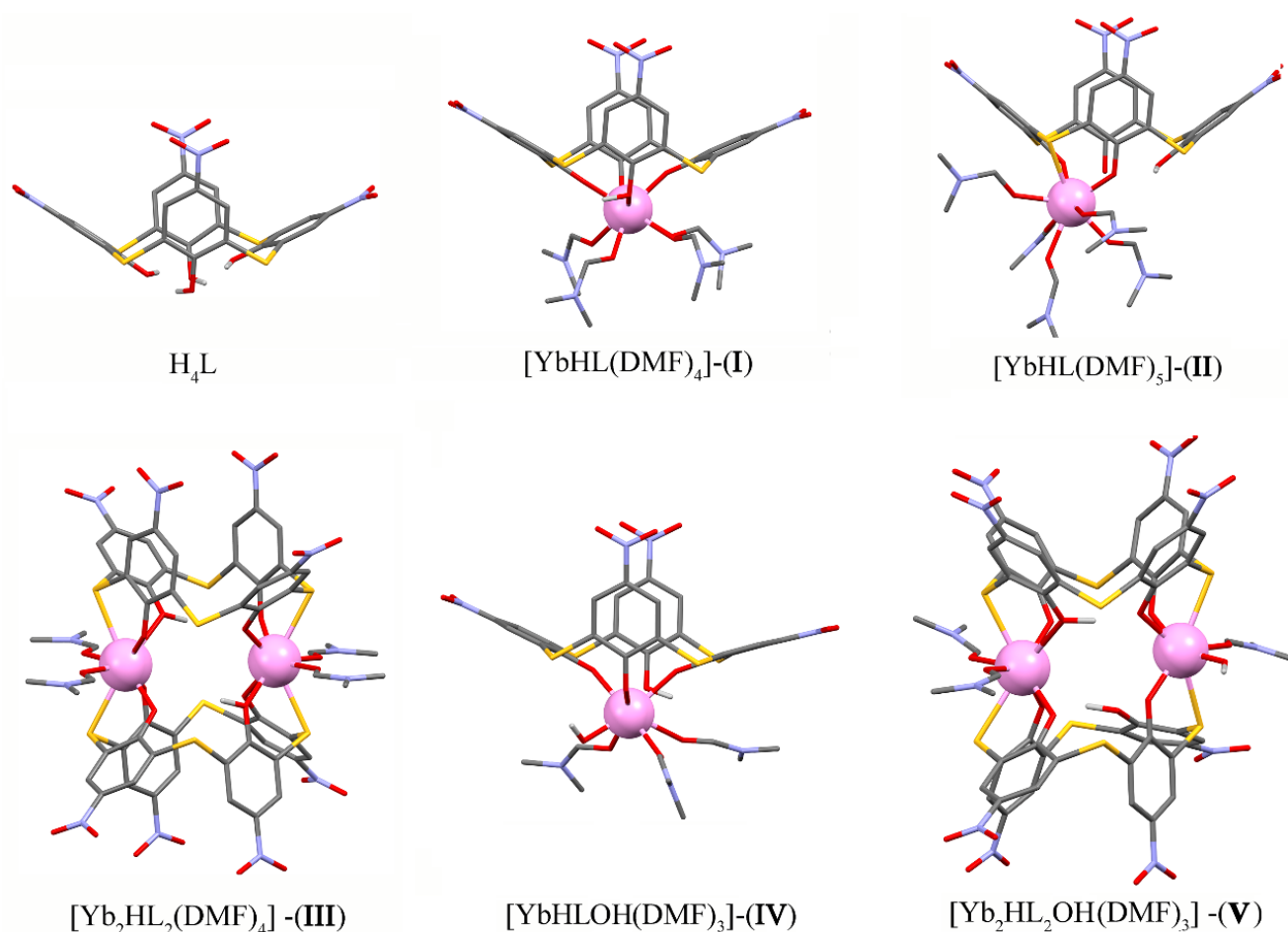
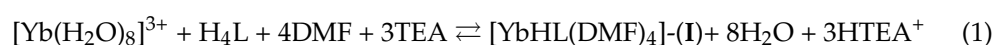
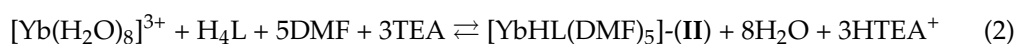


Figure 8. DFT-optimized structures of ligand $\text{H}_4\text{L}(3)$ and its Yb^{3+} complexes. Only hydrogen atoms of phenolic groups are shown for clarity.

The formation of $[\text{YbHL}(\text{DMF})_4]$ -**(I)** and $[\text{YbHL}(\text{DMF})_5]$ -**(II)** from the aqua complex $[\text{Yb}(\text{H}_2\text{O})_8]^{3+}$ can be designated by Equations (1) and (2), where the Yb^{3+} coordination sphere is saturated by four and five DMF molecules, correspondingly:





The complexes (I–II) can undergo transformation into the 2:2 complex (III) (Figure 8) in accordance with Equations (3) and (4):

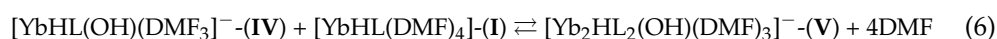


The thermochemical parameters of complexes I, II and III are collected in Table 2. The ΔG^0_{298} -values of monomeric complexes (I,II) formation indicate that they are thermodynamically favorable and mainly provided by the enthalpy contribution (Table 2). However, the dimeric complex formation (equilibriums 3, 4) is an entropically driven process, which differentiates it from the formation of monomeric complexes (I,II). The 2:2 complex formation undergoes coordination of each Yb^{3+} ion via two oxygen and one sulfur atom of H_4L (3), with further saturation of the coordination sphere of Yb^{3+} by two DMF molecules (structure $[\text{Yb}_2\text{HL}_2(\text{DMF})_4]-(\text{III})$ in Figure 8).

Table 2. The calculated thermochemical parameters (ΔH^0_{298} , ΔS^0_{298} and ΔG^0_{298}) of formation of complexes I–V with ligand H_4L (3) in the DMF solutions.

Reaction	Composition	ΔH^0_{298} , kJ	ΔS^0_{298} , J/K	ΔG^0_{298} , kJ
1	$[\text{YbHL}(\text{DMF})_4]-(\text{I})$	−234.1	157.2	−281.0
2	$[\text{YbHL}(\text{DMF})_5]-(\text{II})$	−232.8	61.3	−251.1
3	$[\text{Yb}_2\text{HL}_2(\text{DMF})_4]-(\text{III})$	41.1	217.3	−23.7
4	$[\text{Yb}_2\text{HL}_2(\text{DMF})_4]-(\text{III})$	35.9	400.5	−83.4
5	$[\text{YbHL}(\text{OH})(\text{DMF})_3]-(\text{IV})$	−193.3	157.2	−240.1
6	$[\text{Yb}_2\text{HL}_2(\text{OH})(\text{DMF})_3]-(\text{V})$	−27.0	99.7	−56.7

Lanthanide contraction may be the reason for specificity in the coordinative behavior of Yb^{3+} or Lu^{3+} versus their counterparts from the beginning and middle of the lanthanide series. The specificity is in the enhanced acidity of the inner-sphere water molecules, in turn resulting in their transformation into hydroxyls. The formation of the hydroxyl-containing complex forms $[\text{YbHL}(\text{OH})(\text{DMF})_3]-(\text{IV})$ and $[\text{Yb}_2\text{HL}_2(\text{OH})(\text{DMF})_3]-(\text{V})$ in the presence of TEA can be described by the following equilibriums:



In accordance with the ΔG^0_{298} -values (Table 2), the formation of hydroxy-form (IV) is less profitable in comparison with complexes (I) and (II) in the solution. However, the assembly of $[\text{YbHL}(\text{OH})(\text{DMF})_3]-(\text{IV})$ and $[\text{YbHL}(\text{DMF})_4]-(\text{I})$ into $[\text{Yb}_2\text{HL}_2(\text{OH})(\text{DMF})_3]-(\text{V})$ is both thermodynamically favorable and entropically driven (Table 2). Thus, complex forms III and V are more thermodynamically favorable than I, II and IV. Nevertheless, the NMR diffusion results (Table 1) reveal that the aforesaid complex forms are in equilibrium with the diverse monomeric complex forms.

2.6. Luminescence Spectroscopy

The complex formation in the solutions is followed by the sensitizing of Yb^{3+} -centered luminescence derived from ${}^2\text{F}_{5/2} \rightarrow {}^2\text{F}_{7/2}$ transition, with the main emission band centered at 980 nm and the secondary lines at 971, 996, 1025 and 1040 nm arisen from the main crystal field splitting (Figure 9) [16,17,51]. The spectra in Figure 9 demonstrate that the Yb^{3+} -centered luminescence is the greatest for the complexes with *p*-nitro- and *p*-bromo-substituted thiacalix[4]arenes H_4L (2,3) versus the complex with H_4L (1). The intensity ratios of the bands at 971 and 996 nm, as well as of those at 1025 and 1040 nm, are well-known for their sensitivity to any changes in the inner-sphere ligand environment of Yb^{3+} ions [51]. The ratios at 971 and 996 nm deviate within 1.56–1.72 for the studied ligands, while the

ratio of the lower energy luminescence bands (1025 and 1040 nm) is somewhat greater for the complexes with ligand **3** versus those with **1** and **2**, which argues for some peculiarity in the inner-sphere environment of Yb^{3+} in the case of **3**. It is worth noting the equilibration of the above-mentioned 2:2, 1:1 and 2:1 complexes as the factor influencing the inner-sphere environment of Yb^{3+} ions in the complexes with ligands **2** and **3**. Thus, the aforesaid deviation between the spectral patterns of the complexes and ligands **2** and **3** (Figure 9) can be explained by the different ratios of the dimeric to monomeric complex forms.

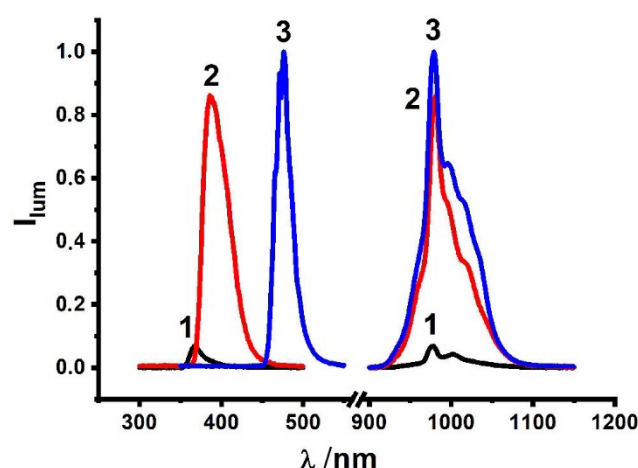


Figure 9. Excitation and emission spectra of Yb^{3+} complexes with H_4L (**1–3**) in the present TEA in DMF solutions.

The average excited state lifetime (τ_{av}) values of Yb^{3+} in the complexes with ligands **2** and **3** are 17.68 μs and 23.58 μs (Table 3). The τ -value of the complex with **1** is significantly shorter; thus, its correct measuring lies out of the present work's scope since the lowest limit of correct lifetime estimation is around 10 μs for a flash lamp used as the excitation source. Altogether, these facts argue for the small number of solvent molecules in the inner sphere environment of Yb^{3+} ion for $\text{H}_4\text{L}(\mathbf{2,3})$ complexes, pointing to the significant contribution of 2:2 form in contrast to 1:1 form for $\text{H}_4\text{L}(\mathbf{1})$. The steady state intensities of the complexes correlate with their excited state lifetimes (Table 3), thus indicating that the radiationless losses are significantly lower for the complexes with $\text{H}_4\text{L}(\mathbf{2,3})$ versus those with $\text{H}_4\text{L}(\mathbf{1})$. It is worth noting that the similarity in τ_{av} -values of Yb^{3+} in the complexes with ligands **2** and **3** allows to exclude the significant dissipation of the excitation energy in $\text{H}_4\text{L}(\text{R} = \text{NO}_2)$ caused by the presence of the nitro-substituents as it was found for the lanthanide complexes with nitrobenzoates [35].

Table 3. Energies of lowest triplet states (T_1) of ligands $\text{H}_4\text{L}(\mathbf{1–3})$ in the 2:2 complexes, average lifetimes of the Yb^{3+} -centered luminescence ($\langle\tau\rangle^1$) and ligand-centered phosphorescence of the Gd^{3+} complexes ($\langle\tau\rangle^2$).

H_4L	Triplet Level, T_1 λ , nm (ν , cm^{-1}) at 146 K	$\langle\tau\rangle^1$ (μs) at 298 K	$\langle\tau\rangle^2$ (μs) at 146 K
1	417 (23,981) ³	-	1437 ³
2	458 (21,834) ⁴	24	301 ⁴
3	567 (17,637)	18	421

¹ for Yb^{3+} complexes. ² for Gd^{3+} complexes. ^{3,4} the previously reported values [7,8].

The excitation spectra of the complexes also reveal the difference between the ligands $\text{H}_4\text{L}(\mathbf{1–3})$ (Figure 9). In particular, the maximums of the excitation bands exhibit red shifting, which increases in the following series: $\text{H}_4\text{L}(\mathbf{1})$ (367 nm) < $\text{H}_4\text{L}(\mathbf{2})$ (386 nm) < $\text{H}_4\text{L}(\mathbf{3})$ (476 nm).

Low temperature phosphorescence measurements of $[\text{Gd}_2\text{L}_2]^{2-}$ for $\text{H}_4\text{L}(\mathbf{3})$ were performed to evaluate the energy of the triplet level at 567 nm ($17,637\text{ cm}^{-1}$) (Figure S8) and average lifetimes of the ligand-centered phosphorescence of the Gd^{3+} ($\langle\tau\rangle = 753\text{ }\mu\text{s}$). The value is much lower than the previously reported triplet level energies for the complexes with ligands $\text{H}_4\text{L}(\mathbf{1})$ and $\text{H}_4\text{L}(\mathbf{2})$ (417 nm ($23,981\text{ cm}^{-1}$) and 458 nm ($21,834\text{ cm}^{-1}$), accordingly [8]. The energies of the triplet levels of the ligands increase in the following series: $\text{H}_4\text{L}(\mathbf{1})$ (417 nm) < $\text{H}_4\text{L}(\mathbf{2})$ (458 nm) < $\text{H}_4\text{L}(\mathbf{3})$ (567 nm) (Table 3), which is in good correlation with the above-mentioned red-shifting of the excitation bands.

Visible light excitation is especially important for NIR emitting materials employed in biochemistry and cell biology since living tissues are sensitive to UV irritation [34]. This indicates that the advantage of $\text{H}_4\text{L}(\mathbf{3})$ versus $\text{H}_4\text{L}(\mathbf{2})$ is the excitation of the bright NIR-luminescence by the lower energy irradiation. Nevertheless, the energy of the triplet level provides a relatively small impact on the Yb^{3+} -luminescence of the complexes with ligands $\text{H}_4\text{L}(\mathbf{2},\mathbf{3})$. This argues for the effect of the upper-rim substituents $\text{R} = \text{NO}_2$, Br on the restricted flexibility of the outer-sphere environment of Yb^{3+} ions versus ligand $\text{H}_4\text{L}(\mathbf{1}, \text{R} = \text{H})$ as the main reason for the longer excited state lifetimes (Table 3) and brighter NIR luminescence (Figure 9).

3. Materials and Methods

N,N-dimethylformamide (DMF) (Acros Organics) was distilled over P_2O_5 . CDCl_3 (99.8% isotopic purity) and $\text{DMSO-}d^6$ (99.5% isotopic purity) from Aldrich were used for NMR spectroscopy. Triethylamine (Acros Organics), terbium nitrate ($\text{Yb}(\text{NO}_3)_3 \cdot 5\text{H}_2\text{O}$) and terbium chloride ($\text{YbCl}_3 \cdot 6\text{H}_2\text{O}$) (Sigma-Aldrich) were used as commercially received without further purification. The structural formulae of the investigated compounds are shown in Figure 1. Tetrathiacalix[4]arenes **1** [52], **2** [53] and **3** [12] were obtained as described in the literature.

3.1. Synthesis of Complex 3 with YbCl_3

The 2.85 mL of 4.5 mM solution of $\text{H}_4\text{L}(\mathbf{3})$ in DMF was mixed with 0.135 mL (0.1 M) of solution of ytterbium chloride hexahydrate in DMF. To this mixture, 0.015 mL (7.2 mM) of solution of TEA was added. The resulting solution was stored at room temperature for a few months and resulted in formation of yellowish needle-like crystals, which have been used for X-ray analysis.

3.2. Physical Measurements and Methods

Detailed descriptions of physical measurements and methods (electronic absorption, NMR experiments, MALDI-TOF mass spectrometry, crystal structure data, luminescence spectroscopy and quantum-chemical modeling) are presented in Supplementary Materials.

4. Conclusions

The present work revealed the impact of the bromo- and nitro-substituents embedded at the upper rim of thiacalix[4]arenes on a supramolecular package in crystals and solution behavior of both tetra-bromo and tetra-nitrothiacalix[4]arenes as well as their ytterbium complexes. It was shown that the upper-rim substituents ($\text{R} = \text{Br}, \text{NO}_2$) enhance deprotonation of the phenolic rims and generate the unusual inclusive self-assembly of H_3L^- ($\text{R} = \text{Br}$), revealed through single-crystal XRD analysis. Similar to non-substituted thiacalix[4]arenes, both tetra-bromo and tetra-nitrothiacalix[4]arenes coordinate Yb^{3+} ions into 1:1, 2:2 and 2:1 ($\text{Yb}:\text{L}$) complex forms, but the antenna effect of the thiacalix[4]arene-based ligands on the Yb^{3+} -centered luminescence is greatly enhanced by the bromo- and nitro-substituents. Quantum chemical study revealed thermodynamic favorableness of the formation of dimeric 2:2 ($\text{Yb}:[\text{HL}]^-$) complexes with a rigid structure as one of the reasons for efficient sensitizing of the Yb^{3+} luminescence. X-ray analysis of the single crystal separated from the basified DMF solutions of YbCl_3 and H_4L ($\text{R} = \text{NO}_2$) revealed transformation of the dimeric complexes into $[\text{4Yb}^{3+}:\text{2L}^{4-}]$ ones with a cubane-like cluster structure.

Analysis of the time-resolved luminescence in correlation with the triplet energy levels revealed peculiarity in the antenna effect of $H_4L(R = NO_2)$, which is efficient sensitizing of the Yb^{3+} luminescence by the triplet level of the ligand at 588 nm arisen from the ILCT without a significant decrease in the lifetime of the excited state caused by dissipation of an excitation energy in $H_4L(R = NO_2)$. However, the tetra-brominated ligand provides similar sensitizing due to the smaller radiationless losses of the ligand environment. Nevertheless, the red-shifting of the excitation wavelengths from 360–380 and 370–420 nm for $H_4L(R = H, Br)$ to 460–500 nm for $H_4L(R = NO_2)$ provides an advantage of $H_4L(R = NO_2)$ versus $H_4L(R = H, Br)$ in further bio-applications.

Supplementary Materials: The following supporting information can be downloaded at <https://www.mdpi.com/article/10.3390/molecules27206793/s1>: Structural formulae of the investigated compounds $H_4L(1-3)$; NMR spectroscopy [54]; crystal structure data [55–64]; the crystal structure data and the parameters of the intra- and intermolecular interactions for $H_3L(2)^- \cdot (CH_3)_2NH_2^+ \cdot DMF$; crystal structure data and parameters of the intermolecular interactions for complex $H_4L(3)$ with $YbCl_3$ [65], UV-absorption spectroscopy; MALDI-TOF mass spectrometry; luminescence spectroscopy and determination of the T_1 state energy of the ligand $H_4L(3)$ in its Gd^{3+} complex [66]; computational methodology [67–80]; optimized coordinates of atoms for ligand $H_4L(3)$ and its Yb^{3+} complexes.

Author Contributions: Conceptualization, writing, S.N.P. and A.R.M.; luminescence investigation, S.N.S.; NIR luminescence investigation, R.R.Z. and A.P.D.; NMR studies, V.V.S.; organic synthesis, G.S.M.; X-ray analysis, M.D. and A.T.G.; MALDI-TOF mass spectrometry, D.N.B. and V.M.B.; time-resolved luminescence and decay kinetics experiments, D.V.L.; quantum-chemical calculation, A.N.M. and A.M.K. All authors have read and agreed to the published version of the manuscript.

Funding: Crystallographic analysis of complex $H_4L(3)$ with Yb^{3+} ions was carried out by Michal Dusek with use of infrastructure supported by the Operational Programme Research, Development and Education financed by the European Structural and Investment Funds and the Czech Ministry of Education, Youth and Sports (Project No. SOLID21 CZ.02.1.01/0.0/0.0/16_019/0000760). Luminescence spectra of Yb^{3+} complexes with $H_4L(1-3)$ were recorded by Alexey Dovzhenko with support of Kazan Federal University Strategic Academic Leadership Program (PRIORITY-2030). The other part of the work was funded by the Government assignment for FRC Kazan Scientific Center of RAS (S.N.P., S.N.S., R.R.Z., V.V.S., A.T.G., D.N.B., D.V.L., G.S.M., V.M.B. and A.R.M.).

Institutional Review Board Statement: Not applicable.

Informed Consent Statement: Not applicable.

Data Availability Statement: The data presented in this study are available in Supplementary Materials.

Acknowledgments: The measurements have been carried out using the equipment of Distributed Spectral-Analytical Center of Shared Facilities for Study of Structure, Composition and Properties of Substances and Materials of FRC Kazan Scientific Center of RAS.

Conflicts of Interest: The authors declare that they have no known competing financial interest or personal relationship that could appear to have influenced the work reported in this paper.

Sample Availability: Samples of all obtained compounds are available from the authors.

References

1. Podyachev, S.N.; Zairov, R.R.; Mustafina, A.R. 1,3-Diketone calix [4]arene derivatives—A new type of versatile ligands for metal complexes and nanoparticles. *Molecules* **2021**, *26*, 1214. [[CrossRef](#)] [[PubMed](#)]
2. Massi, M.; Odgen, M.I.; Odgen, M.I. Luminescent lanthanoid calixarene complexes and materials. *Materials* **2017**, *10*, 1369. [[CrossRef](#)]
3. Danil de Namor, A.F.; Cleverley, R.M.; Zapata-Ormachea, M.L. Thermodynamics of Calixarene Chemistry. *Chem. Rev.* **1998**, *98*, 2495–2526. [[CrossRef](#)] [[PubMed](#)]
4. Padnya, P.; Shibaeva, K.; Arsenyev, M.; Baryshnikova, S.; Terenteva, O.; Shiabiev, I.; Khannanov, A.; Boldyrev, A.; Gerasimov, A.; Grishaev, D.; et al. Catechol-containing schiff bases on thiacalixarene: Synthesis, copper (II) recognition, and formation of organic-inorganic copper-based materials. *Molecules* **2021**, *26*, 2334. [[CrossRef](#)] [[PubMed](#)]
5. Mandolini, L.; Ungaro, R. *>Calixarenes in Action*; Mandolini, L., Ungaro, R., Eds.; Imperial College Press: London, UK, 2000; ISBN 978-1-86094-194-8.

6. *Macrocyclic Chemistry: Current Trends and Future Perspectives*; Gloe, K. (Ed.) Springer: Dordrecht, The Netherlands, 2005; ISBN 9781402033643.
7. Podyachev, S.N.; Sudakova, S.N.; Nagimov, R.N.; Lapaev, D.V.; Masliy, A.N.; Syakaev, V.V.; Bazanova, O.B.; Gimazetdinova, G.S.; Babaev, V.M.; Kuznetsov, A.M.; et al. Structural and photophysical properties of Tb³⁺-Tetra-1,3-diketonate complexes controlled by calix [4]arene-tetrathiacalix [4]arene scaffolds. *Dalton Trans.* **2019**, *48*, 3930–3940. [[CrossRef](#)]
8. Podyachev, S.N.; Sudakova, S.N.; Nagimov, R.N.; Masliy, A.N.; Syakaev, V.V.; Lapaev, D.V.; Buzyurova, D.N.; Babaev, V.M.; Gimazetdinova, G.S.; Kuznetsov, A.M.; et al. A simple synthetic approach to enhance the thermal luminescence sensitivity of Tb³⁺ complexes with thiacalix [4]arene derivatives through upper-rim bromination. *Dalton Trans.* **2020**, *49*, 8298–8313. [[CrossRef](#)] [[PubMed](#)]
9. Iki, N. Designing strategies for supramolecular luminescent complex of lanthanide-heterometal assembly. *Supramol. Chem.* **2011**, *23*, 160–168. [[CrossRef](#)]
10. Tian, H.-W.; Liu, Y.-C.; Guo, D.-S. Assembling features of calixarene-based amphiphiles and supra-amphiphiles. *Mater. Chem. Front.* **2020**, *4*, 46–98. [[CrossRef](#)]
11. Desroches, C.; Parola, S.; Vocanson, F.; Perrin, M.; Lamartine, R.; Létoffé, J.-M.; Bouix, J. Nitration of thiacalix [4]arene using nitrosium nitrate complexes: Synthesis and characterization of tetranitro-, tetraamino-, and tetra(4-pyridylimino)tetrahydroxythiacalix [4]arene. *New J. Chem.* **2002**, *26*, 651–655. [[CrossRef](#)]
12. Hu, X.; Zhu, Z.; Shen, T.; Shi, X.; Ren, J.; Sun, Q. Synthesis of the tetranitro derivative of thiacalix [4]arene and its acid-base properties. *Can. J. Chem.* **2004**, *82*, 1266–1270. [[CrossRef](#)]
13. Hu, X.; Shi, H.; Shi, X.; Zhu, Z.; Sun, Q.; Li, Y.; Yang, H. Selective nitration of thiacalix [4]arene and an investigation of its acid-base properties with a chemometric method. *Bull. Chem. Soc. Jpn.* **2005**, *78*, 138–141. [[CrossRef](#)]
14. Muravev, A.; Gerasimova, T.; Fayzullin, R.; Babaeva, O.; Rizvanov, I.; Khamatgalimov, A.; Kadirov, M.; Katsyuba, S.; Litvinov, I.; Latypov, S.; et al. Thermally stable nitrothiacalixarene chromophores: Conformational study and aggregation behavior. *Int. J. Mol. Sci.* **2020**, *21*, 6916. [[CrossRef](#)]
15. Liu, Q.; Zou, X.; Shi, Y.; Shen, B.; Cao, C.; Cheng, S.; Feng, W.; Li, F. An efficient dye-sensitized NIR emissive lanthanide nanomaterial and its application in fluorescence-guided peritumoral lymph node dissection. *Nanoscale* **2018**, *10*, 12573–12581. [[CrossRef](#)]
16. Bünzli, J.-C.G. Lanthanide light for biology and medical diagnosis. *J. Lumin.* **2016**, *170*, 866–878. [[CrossRef](#)]
17. Eliseeva, S.V.; Bünzli, J.-C.G. Lanthanide luminescence for functional materials and bio-sciences. *Chem. Soc. Rev.* **2010**, *39*, 189–227. [[CrossRef](#)]
18. Nunes, L.R.R.; Labaki, H.P.; Caixeta, F.J.; Gonçalves, R.R. Yb³⁺ influence on NIR emission from Pr³⁺-doped spherical yttria nanoparticles for advances in NIR I and NIR II biological windows. *J. Lumin.* **2022**, *241*, 118485. [[CrossRef](#)]
19. Kovalenko, A.D.; Pavlov, A.A.; Ustinovich, I.D.; Kalyakina, A.S.; Goloveshkin, A.S.; Marciniak, Ł.; Lepnev, L.S.; Burlov, A.S.; Schepers, U.; Bräse, S.; et al. Highly NIR-emitting ytterbium complexes containing 2-(tosylaminobenzylidene)- N -benzoylhydrazone anions: Structure in solution and use for bioimaging. *Dalton Trans.* **2021**, *50*, 3786–3791. [[CrossRef](#)]
20. Ning, Y.; Zhu, M.; Zhang, J.-L. Near-infrared (NIR) lanthanide molecular probes for bioimaging and biosensing. *Coord. Chem. Rev.* **2019**, *399*, 213028. [[CrossRef](#)]
21. Kang, X.; Li, C.; Cheng, Z.; Ma, P.; Hou, Z.; Lin, J. Lanthanide—Doped hollow nanomaterials as theranostic agents. *WIREs Nanomed. Nanobiotechnol.* **2014**, *6*, 80–101. [[CrossRef](#)] [[PubMed](#)]
22. Sui, J.; Liu, G.; Song, Y.; Li, D.; Dong, X.; Wang, J.; Yu, W. Integrating photoluminescence, magnetism and thermal conversion for potential photothermal therapy and dual-modal bioimaging. *J. Colloid Interface Sci.* **2018**, *510*, 292–301. [[CrossRef](#)] [[PubMed](#)]
23. Comby, S.; Bünzli, J.-C.G. Lanthanide near-infrared luminescence in molecular probes and devices. In *Handbook on the Physics and Chemistry of Rare Earths*; Gschneidner, K.A.J., Bünzli, J.-C.G., Pecharsky, V.K., Eds.; Elsevier Science: Amsterdam, The Netherlands, 2007; pp. 217–470.
24. Carnall, W.T. The absorption and fluorescence spectra of rare earth ions in solution. In *Handbook on the Physics and Chemistry of Rare Earths*; Gschneidner, K.A.J., Eyring, L., Eds.; Elsevier: Amsterdam, The Netherlands, 1979; pp. 171–208.
25. Shavaleev, N.M.; Scopelliti, R.; Gumy, F.; Bünzli, J.-C.G. Surprisingly bright near-infrared luminescence and short radiative lifetimes of ytterbium in hetero-binuclear Yb–Na chelates. *Inorg. Chem.* **2009**, *48*, 7937–7946. [[CrossRef](#)] [[PubMed](#)]
26. Shavaleev, N.M.; Scopelliti, R.; Gumy, F.; Bünzli, J.-C.G. Modulating the near-infrared luminescence of neodymium and ytterbium complexes with tridentate ligands based on benzoxazole-substituted 8-hydroxyquinolines. *Inorg. Chem.* **2009**, *48*, 2908–2918. [[CrossRef](#)] [[PubMed](#)]
27. Kim, J.H.; Lepnev, L.S.; Utochnikova, V.V. Dual vis-NIR emissive bimetallic naphthoates of Eu–Yb–Gd: A new approach toward Yb luminescence intensity increase through Eu → Yb energy transfer. *Phys. Chem. Chem. Phys.* **2021**, *23*, 7213–7219. [[CrossRef](#)]
28. Zairov, R.R.; Dovzhenko, A.P.; Sapunova, A.S.; Voloshina, A.D.; Tatarinov, D.A.; Nizameev, I.R.; Gubaidullin, A.T.; Petrov, K.A.; Enrichi, F.; Vomiero, A.; et al. Dual red-NIR luminescent Eu Yb heterolanthanide nanoparticles as promising basis for cellular imaging and sensing. *Mater. Sci. Eng. C* **2019**, *105*, 110057. [[CrossRef](#)]
29. Fedorenko, S.; Gilmanova, D.; Mukhametshina, A.; Nizameev, I.; Kholin, K.; Akhmadeev, B.; Voloshina, A.; Sapunova, A.; Kuznetsova, S.; Daminova, A.; et al. Silica nanoparticles with dual visible–NIR luminescence affected by silica confinement of Tb(III) and Yb(III) complexes for cellular imaging application. *J. Mater. Sci.* **2019**, *54*, 9140–9154. [[CrossRef](#)]

30. Iki, N.; Hiro-oka, S.; Nakamura, M.; Tanaka, T.; Hoshino, H. Kinetically stable LnIII complexes comprising a trinuclear core sandwiched between two thiacalix [4]arene ligands self-assembled in water (LnIII = NdIII, YbIII). *Eur. J. Inorg. Chem.* **2012**, *2012*, 3541–3545. [[CrossRef](#)]
31. Iki, N.; Tanaka, T.; Hiro-oka, S.; Shinoda, K. Self-assembly of a trilanthanide(III) Ccre sandwiched between two thiacalix [4]arene ligands. *Eur. J. Inorg. Chem.* **2016**, *2016*, 5020–5027. [[CrossRef](#)]
32. Karashimada, R.; Iki, N. Thiacalixarene assembled heterotrinary lanthanide clusters comprising TbIII and YbIII enable f–f communication to enhance Yb III-centred luminescence. *Chem. Commun.* **2016**, *52*, 3139–3142. [[CrossRef](#)]
33. Peng, Y.; Fu, S.; Liu, H.; Lucia, L.A. Accurately determining esterase activity via the isosbestic point of p-nitrophenol. *BioResources* **2016**, *11*, 10099–10111. [[CrossRef](#)]
34. Zhang, Z.; Zhou, Y.; Li, H.; Gao, T.; Yan, P. Visible light sensitized near-infrared luminescence of ytterbium via ILCT states in quadruple-stranded helicates. *Dalton Trans.* **2019**, *48*, 4026–4034. [[CrossRef](#)]
35. Tsaryuk, V.; Kudryashova, V.; Gawryszewska, P.; Szostak, R.; Vologzhanina, A.; Zhuravlev, K.; Klemenkova, Z.; Legendziewicz, J.; Zolin, V. Structures, luminescence and vibrational spectroscopy of europium and terbium nitro- and dinitro-substituted benzoates. Nitro groups as quenchers of Ln³⁺ luminescence. *J. Photochem. Photobiol. A Chem.* **2012**, *239*, 37–46. [[CrossRef](#)]
36. Desiraju, G.R.; Ho, P.S.; Kloo, L.; Legon, A.C.; Marquardt, R.; Metrangolo, P.; Politzer, P.; Resnati, G.; Rissanen, K. Definition of the halogen bond (IUPAC Recommendations 2013). *Pure Appl. Chem.* **2013**, *85*, 1711–1713. [[CrossRef](#)]
37. Spek, A.L. Single-crystal structure validation with the program PLATON. *J. Appl. Crystallogr.* **2003**, *36*, 7–13. [[CrossRef](#)]
38. Wang, Y.; Miao, X.; Deng, W. Halogen bonds fabricate 2D molecular self-assembled nanostructures by scanning tunneling microscopy. *Crystals* **2020**, *10*, 1057. [[CrossRef](#)]
39. Puttreddy, R.; Beyeh, N.K.; Ras, R.H.A.; Trant, J.F.; Rissanen, K. *Endo-/exo-* and halogen-bonded complexes of conformationally rigid C-ethyl-2-bromoresorcinarene and aromatic *N*-oxides. *CrystEngComm*. **2017**, *19*, 4312–4320. [[CrossRef](#)]
40. Cao, J.; Yan, X.; He, W.; Li, X.; Li, Z.; Mo, Y.; Liu, M.; Jiang, Y.-B. C–I ··· π Halogen bonding driven supramolecular helix of bilateral *N*-amidothiouras bearing β -Turns. *J. Am. Chem. Soc.* **2017**, *139*, 6605–6610. [[CrossRef](#)]
41. Twum, K.; Rissanen, K.; Beyeh, N.K. Recent advances in halogen bonded assemblies with resorcin [4]arenes. *Chem. Rec.* **2021**, *21*, 386–395. [[CrossRef](#)]
42. Kennedy, S.R.; Main, M.U.; Pulham, C.R.; Ling, I.; Dalgarno, S.J. A self-assembled nanotube supported by halogen bonding interactions. *CrystEngComm* **2019**, *21*, 786–790. [[CrossRef](#)]
43. Ferreira da Rosa, P.P.; Kitagawa, Y.; Hasegawa, Y. Luminescent lanthanide complex with seven-coordination geometry. *Coord. Chem. Rev.* **2020**, *406*, 213153. [[CrossRef](#)]
44. Kajiwara, T.; Iki, N.; Yamashita, M. Transition metal and lanthanide cluster complexes constructed with thiacalix[n]arene and its derivatives. *Coord. Chem. Rev.* **2007**, *251*, 1734–1746. [[CrossRef](#)]
45. Kajiwara, T.; Katagiri, K.; Hasegawa, M.; Ishii, A.; Ferbinteanu, M.; Takaishi, S.; Ito, T.; Yamashita, M.; Iki, N. Conformation-controlled luminescent properties of lanthanide clusters containing p-tert-butylsulfonycalix [4]arene. *Inorg. Chem.* **2006**, *45*, 4880–4882. [[CrossRef](#)] [[PubMed](#)]
46. Altieri, A.S.; Hinton, D.P.; Byrd, R.A. Association of biomolecular systems via pulsed field gradient NMR self-diffusion measurements. *J. Am. Chem. Soc.* **1995**, *117*, 7566–7567. [[CrossRef](#)]
47. Krishnan, V.V. Determination of oligomeric state of proteins in solution from pulsed-field-gradient self-diffusion coefficient measurements. A comparison of experimental, theoretical, and hard-sphere approximated values. *J. Magn. Reson.* **1997**, *124*, 468–473. [[CrossRef](#)]
48. Podyachev, S.N.; Sudakova, S.N.; Syakaev, V.V.; Burmakina, N.E.; Shagidullin, R.R.; Morozov, V.I.; Avvakumova, L.V.; Konovalov, A.I. Synthesis and properties of potassium salts of per-O-carboxymethyl-calix [4]pyrogallols and their complexes with Cu²⁺, Fe³⁺, and La³⁺. *Russ. Chem. Bull.* **2009**, *58*, 80–88. [[CrossRef](#)]
49. Shannon, R.D. Revised effective ionic radii and systematic studies of interatomic distances in halides and chalcogenides. *Acta Crystallogr. Sect. A* **1976**, *32*, 751–767. [[CrossRef](#)]
50. Cotton, S.A. Establishing coordination numbers for the lanthanides in simple complexes. *Comptes Rendus Chim.* **2005**, *8*, 129–145. [[CrossRef](#)]
51. Shuvaev, S.; Parker, D. A near-IR luminescent ratiometric ytterbium pH probe. *Dalton Trans.* **2019**, *48*, 4471–4473. [[CrossRef](#)]
52. Higuchi, Y. Fluorescent chemo-sensor for metal cations based on thiacalix[4]arenes modified with dansyl moieties at the lower rim. *Tetrahedron* **2000**, *56*, 4659–4666. [[CrossRef](#)]
53. Desroches, C.; Lopes, C.; Kessler, V.; Parola, S. Design and synthesis of multifunctional thiacalixarenes and related metal derivatives for the preparation of sol–gel hybrid materials with non-linear optical properties. *Dalton Trans.* **2003**, *2003*, 2085–2092. [[CrossRef](#)]
54. Wu, D.; Chen, A.; Johnson, C. An Improved Diffusion-Ordered Spectroscopy Experiment Incorporating Bipolar-Gradient Pulses. *J. Magn. Reson. Ser. A* **1995**, *115*, 260–264. [[CrossRef](#)]
55. Sheldrick, G.M. *SADABS-2012/1. Bruker/Siemens Area Detector Absorption Correction Program*; Bruker AXS Inc.: Madison, WI, USA, 2012.
56. Sheldrick, G.M. M.: *SHELXTL. Structure Determination Software Suite, SHELXTL, Structure Determination Software Suite, v. 6.1*; Bruker AXS Inc.: Madison, WI, USA, 2000.
57. APEX3. *Crystallography Software Suite, Version 2018.7-2*; Bruker AXS Inc.: Madison, WI, USA, 2016.
58. Farrugia, L.J. *WinGX suite for small-molecule single-crystal crystallography. J. Appl. Crystallogr.* **1999**, *32*, 837–838. [[CrossRef](#)]

59. Macrae, C.F.; Sovago, I.; Cottrell, S.J.; Galek, P.T.A.; McCabe, P.; Pidcock, E.; Platings, M.; Shields, G.P.; Stevens, J.S.; Towler, M.; et al. *Mercury 4.0: From visualization to analysis, design and prediction*. *J. Appl. Crystallogr.* **2020**, *53*, 226–235. [[CrossRef](#)] [[PubMed](#)]
60. Rigaku Oxford Diffraction, *CrysAlisPro Software system, Version 1.171.42.51 2022*; Rigaku Corporation: Oxford, UK, 2015.
61. Sheldrick, G.M. *SHELXT—Integrated space-group and crystal-structure determination*. *Acta Crystallogr. Sect. A: Found. Adv.* **2015**, *71*, 3–8. [[CrossRef](#)] [[PubMed](#)]
62. Palatinus, L.; Chapuis, G. *SUPERFLIP—A computer program for the solution of crystal structures by charge flipping in arbitrary dimensions*. *J. Appl. Crystallogr.* **2007**, *40*, 786–790. [[CrossRef](#)]
63. Petříček, V.; Dušek, M.; Palatinus, L. Crystallographic Computing System JANA2006: General features. *Z. Für Krist. Cryst. Mater.* **2014**, *229*, 345–352. [[CrossRef](#)]
64. Putz, H.; Brandenburg, K. *Diamond—Crystal and Molecular Structure Visualization, Crystal Impact—H. Putz & K. Brandenburg GbR, Kreuzherrenstr. 102, D-53227 Bonn, Germany*. Available online: <https://www.crystalimpact.de/diamond> (accessed on 24 February 2022).
65. Schomaker, V.; Trueblood, K.N. On the rigid-body motion of molecules in crystals. *Acta Crystallogr. Sect. B Struct. Crystallogr. Cryst. Chem.* **1968**, *24*, 63–76. [[CrossRef](#)]
66. Lapaev, D.V.; Nikiforov, V.G.; Safiullin, G.M.; Galyaviev, I.G.; Dzabarov, V.I.; Knyazev, A.; Lobkov, V.S.; Galyametdinov, Y. Interligand energy transfer in europium(III) mesogenic adducts. *J. Struct. Chem.* **2009**, *50*, 775–781. [[CrossRef](#)]
67. Laikov, D.N. Fast evaluation of density functional exchange-correlation terms using the expansion of the electron density in auxiliary basis sets. *Chem. Phys. Lett.* **1997**, *281*, 151–156. [[CrossRef](#)]
68. Perdew, J.P.; Burke, K.; Ernzerhof, M. Generalized gradient approximation made simple. *Phys. Rev. Lett.* **1996**, *77*, 3865. [[CrossRef](#)]
69. Laikov, D.N. A new class of atomic basis functions for accurate electronic structure calculations of molecules. *Chem. Phys. Lett.* **2005**, *416*, 116–120. [[CrossRef](#)]
70. Bakovets, V.V.; Masliy, A.N.; Kuznetsov, A.M. Formation Thermodynamics of Cucurbit[6]uril Macrocycle Molecules: A Theory Study. *J. Phys. Chem. B* **2008**, *112*, 12010–12013. [[CrossRef](#)] [[PubMed](#)]
71. Podyachev, S.N.; Gubaidullin, A.T.; Syakaev, V.V.; Sudakova, S.N.; Masliy, A.N.; Saifina, A.F.; Burmakina, N.; Kuznetsov, A.M.; Shagidullin, R.R.; Avvakumova, L.V.; et al. Structural characterization and some coordinational aspects of tetrathiacalix[4]arenes functionalized by hydrazide groups. *J. Mol. Struct.* **2010**, *967*, 72–79. [[CrossRef](#)]
72. Podyachev, S.N.; Masliy, A.N.; Semenov, V.E.; Syakaev, V.V.; Sudakova, S.N.; Voronina, J.K.; Ivanov, V.T.; Kuznetsov, A.M.; Gogolashvili, E.L.; Reznik, V.S.; et al. Silver mediated duplex-type complexes of pyrimidinophanes and their acyclic counterparts. *RSC Adv.* **2015**, *5*, 16017–16028. [[CrossRef](#)]
73. Kovalenko, E.; Vilaseca, M.; Díaz-Lobo, M.; Masliy, A.N.; Vicent, C.; Fedin, V.P. Supramolecular Adducts of Cucurbit[7]uril and Amino Acids in the Gas Phase. *J. Am. Soc. Mass Spectrom.* **2015**, *27*, 265–276. [[CrossRef](#)]
74. Grishaeva, T.N.; Masliy, A.; Kuznetsov, A.M. Water structuring inside the cavities of cucurbit[n]urils (n = 5–8): A quantum-chemical forecast. *J. Incl. Phenom. Macrocycl. Chem.* **2017**, *89*, 299–313. [[CrossRef](#)]
75. Kovalenko, E.A.; Pashkina, E.A.; Kanazhevskaya, L.Y.; Masliy, A.N.; Kozlov, V.A. Chemical and biological properties of a supramolecular complex of tuftsin and cucurbit[7]uril. *Int. Immunopharmacol.* **2017**, *47*, 199–205. [[CrossRef](#)]
76. Frisch, M.J.; Trucks, G.W.; Schlegel, H.B.; Scuseria, G.E.; Robb, M.A.; Cheeseman, J.R.; Scalmani, G.; Barone, V.; Petersson, G.A.; Nakatsuji, H.; et al. *Gaussian 09, Revision E.01*; Gaussian, Inc.: Wallingford, CT, USA, 2016.
77. Cancès, E.; Mennucci, B.; Tomasi, J. A new integral equation formalism for the polarizable continuum model: Theoretical background and applications to isotropic and anisotropic dielectrics. *J. Chem. Phys.* **1997**, *107*, 3032–3041. [[CrossRef](#)]
78. Cossi, M.; Barone, V.; Mennucci, B.; Tomasi, J. Ab initio study of ionic solutions by a polarizable continuum dielectric model. *Chem. Phys. Lett.* **1998**, *286*, 253–260. [[CrossRef](#)]
79. Mennucci, B.; Tomasi, J. Continuum solvation models: A new approach to the problem of solute’s charge distribution and cavity boundaries. *J. Chem. Phys.* **1997**, *106*, 5151–5158. [[CrossRef](#)]
80. Pollak, P.; Weigend, F. Segmented Contracted Error-Consistent Basis Sets of Double- and Triple- ζ Valence Quality for One- and Two-Component Relativistic All-Electron Calculations. *J. Chem. Theory Comput.* **2017**, *13*, 3696–3705. [[CrossRef](#)]